# Lubrication of dislocation glide in forsterite by Mg vacancies: insights from Peierls-Nabarro modeling

Richard Skelton [a,*] and Andrew M. Walker[b]

1    [a] Research School of Earth Sciences, Australian National University, Canberra, ACT, 0200, Australia

2    (ORCID: 0000-0003-1583-2312)

3    [b] School of Earth and Environment, University of Leeds, Leeds, LS2 9JT, UK

4    (ORCID: 0000-0003-3121-3255)

5    * Corresponding author: richard.skelton@anu.edu.au

6    **Abstract**

7    Dislocation glide is an important contributor to the rheology of olivine under conditions of high stress

8    and low to moderate temperature, such as occur in mantle wedges. Interactions between point defects

9    and dislocation core may alter the Peierls stress, $\sigma_p$, and has been suggested that vacancy-related

10    defects may selectively enhance glide on certain slip systems, changing the olivine deformation fabric.

11    In this study, the Peierls-Nabarro model, parameterized by generalized stacking fault (GSF) energies

12    calculated atomistically using empirical interatomic potentials, is used to determine the effect of bare

13    Mg vacancies on the Peierls stresses of [100](010) and [001](010) dislocations in forsterite. Mg

14    vacancies considerably reduce GSF energies and, consequently, $\sigma_p$ for dislocations gliding on (010) in

15    olivine. The magnitude of this decrease depends strongly on dislocation and the type of the lattice site,

16    with vacant M2 sites producing the largest reduction of $\sigma_p$. The [001](010) slip system is found to be

17    more sensitive than the [100](010) slip system to the presence of vacancies. Although, at ambient

18    pressure, $\sigma_p$ is lower for [100](010) than [001](010) edge dislocations, $d\sigma_p/dP$ is greater for [100](010)

19    dislocations, resulting in a change in the preferred slip system at 1.5 GPa. By preferentially lubricating

20    [001](010) glide, Mg vacancies reduce the pressure at which this cross-over occurs. An M2 vacancy

21 concentration at the glide plane of 0.125 defects/site is sufficient to reduce cross-over to 0.7 GPa. This

22 may account for the existence of the B-type olivine deformation fabric in the corners of mantle wedges.

23 **Keywords:** Forsterite; dislocation; Peierls stress; cation vacancies; Peierls-Nabarro modeling

24 **1. Introduction**

25 Forsterite-rich olivine is the dominant component of the Earth's upper mantle, composing ~60-70% of

26 its bulk by volume. Olivine is also the weakest major phase in this region of the Earth's interior, and

27 accordingly controls its rheology. Interpreting seismological models of the Earth's upper mantle in

28 terms of the dynamics of plastic flow thus requires an intimate understanding of the atomic-scale

29 mechanisms that contribute to the deformation of olivine. A number of mechanisms contribute to the

30 rheology of olivine under mantle conditions, such as grain boundary diffusion (e.g. Mei and Kohlstedt,

31 2000); grain boundary sliding, accommodated by either elastic and diffusional relaxation of the grain

32 boundary (Jackson et al., 2014) or dislocation-enabled deformation of individual grains (e.g. Hansen et

33 al., 2011; Hansen et al., 2012ab); dislocation climb (e.g. Goetze and Kohlstedt, 1973); and dislocation

34 glide (e.g. Evans and Goetze, 1979; Katayama and Karato, 2008).

35 Dislocations play a particularly important role in the deformation of olivine under low temperature or

36 moderate to high stress conditions, such as in the mantle wedge above a subducting slab. The strain rate

37 in this creep regime is controlled by the rate of kink-pair nucleation, which depends on the elasticity of

38 the crystal and the intrinsic lattice friction of the glide plane. This latter property is quantified by the

39 Peierls stress, $\sigma_p$, the critical stress required to initiate free glide of a dislocation at 0 K. Defect

40 chemistry can therefore exert an important influence if immobile impurities segregate strongly to

41 dislocation cores and inhibit glide creep by pinning dislocations, a phenomenon called solute drag

42 (Cottrell and Bilby, 1949).

43 Olivine is a plastically anisotropic mineral, and develops a measurable lattice preferred orientation

44 (LPO) when deformed in the dislocation glide-controlled creep regime (e.g. Nicolas and Christensen,

45 1987; Mainprice, 2007; Long and Silver, 2009; Long and Becker, 2010). The dominant slip system for

46 dislocation creep at low pressure is [100](010). Pressure and defect concentration at the glide plane

47 change the dominant slip system of olivine, and much of the variation in seismic wave anisotropy in the

48 upper mantle is explicable in terms of this pressure-induced transition (Mainprice et al., 2005; Ohuchi

49 et al., 2011; Raterron et al., 2016). At high pressure, the dominant slip system is [001](010), as this slip

50 system hardens less in response to increasing pressure than the [100](010) slip system (Raterron et al.,

51 2011; Hilairet et al., 2012).

52 Experimental studies have reported Peierls stresses for olivine, ranging widely from as little as 3.8 GPa

53 (Idrissi et al., 2016) to ~15 GPa (Demouchy et al., 2013), although typical values are in the range 5-10

54 GPa (e.g. Evans and Goetze, 1979; Kranjc et al., 2016; Proietti et al., 2016). The Peierls stress

55 measured in these studies represents a weighted average of the Peierls stresses of the individual slip

56 systems that contribute to the total strain. While $\sigma_p$ has not been measured experimentally for any

57 individual slip system in olivine, this information gap has been partially filled using atomic scale

58 modeling. Mahendran et al. (2017) directly calculated $\sigma_p$ for [001] and [100] screw dislocations gliding

59 on several crystallographic planes. Consistent with experimental observations, they found that [100]

60 (010) glide is easier than [001](010) glide in forsterite, with Peierls stresses of 3.1 and 7.2 GPa,

61 respectively, within the range of Peierls stresses reported from experiments.

62 Hydrogen, probably incorporated into the olivine lattice by protonation of cation vacancies (e.g. Martin

63 and Donnay, 1972; Bai and Kohlstedt, 1993; Kohlstedt et al., 1996; Lemaire et al., 2004), can influence

64 the rheology of olivine under conditions of low-temperature (<1273 K) and high-stress, reducing $\sigma_p$ to

65 1.6-2.9 GPa (Katayama and Karato, 2008). Similarly, the incorporation of water as the

66 "titanoclinohumite" defect, consisting of charge-coupled $\{Ti_M\}^{\cdot\cdot}$ and $\{2H_{Si}\}''$ defects apparently results

67 in a systematic increase in strain rate (Berry et al., 2005; Faul et al., 2016).

68 Protonated cation vacancies also change the preferred slip system in olivine, with the [001](010) slip

69 was preferred over [100](010) slip at moderate water contents (e.g. Jung and Karato, 2001; Jung et al.,

70 2006; Ohuchi et al., 2012). Natural olivine crystals in subduction zone-derived peridotites show this B-

71 type fabric (Mizukami et al., 2004), and 'wet' olivine fabrics have also been found in some peridotites

72 sourced from the deep upper mantle (Katayama et al. 2005). Such a change in preferred slip system

73 may explain the existence of trench-parallel orientation of 'fast' shear-wave polarizations in mantle

74 wedges above subduction zones (Margheriti et al., 1996; Smith et al., 2001), which has previously been

75 attributed to trench-parallel flow. A water-induced change of deformation fabric implies that protonated

76 vacancies have a differential effect on the critical resolved shear stresses (CRSS) of the dominant slip

77 systems, whether by stabilizing dislocation kinks or reducing the Peierls stress.

78 Atomic-scale calculations show that the energy required to create an Mg vacancy is considerably less

79 than that required to create a Si vacancy (Wright and Catlow, 1994; Brodholt, 1997). Similarly,

80 protonated Mg vacancies have lower energies than protonated Si vacancies (Walker et al., 2007). In the

81 Earth's upper mantle, which is $MgSiO_3$-saturated, M-site vacancies in olivine can thus be expected to

82 be many orders of magnitude more abundant than protonated Si vacancies. The predominance of M site

83 vacancies in mantle olivine could be reinforced in oxidized regions of the mantle, as the oxidation of

84 $Fe^{2+}$ to $Fe^{3+}$ may be accompanied by the creation of M-site vacancies to maintain charge neutrality. The

85 two mechanisms for creating mobile M-site vacancies may co-exist, particularly in mantle wedges

86 above subduction zones, which are oxidized by fluid transfer from the subducting slab (Kelley and

87 Cottrell, 2009). High oxygen fugacity has been shown to enhance seismic attenuation in olivine (Cline

88 et al. 2018). The similarly high oxygen fugacities present in the earlier deformation experiments of

89 Faul et al. (2016), produced by the platinum sleeve used to wrap the specimen (Faul et al., 2017), may

90  indicate that oxidizing conditions may indicate that ferric-iron associated vacancies may have a

91  comparable effect to water on the rheology of olivine.

92  In this study we use computational simulations to investigate the possibility that cation vacancies may

93  be able to lubricate dislocation glide in forsterite by reducing the Peierls stress $\sigma_p$., providing a

94  mechanism by which point defects may influence the rheology of this important mantle mineral in the

95  glide-controlled creep regime. Core structures and Peierls stresses are calculated for important slip

96  systems in forsterite using a semi-discrete Peierls-Nabarro (PN; Peierls, 1940; Nabarro, 1947) model.

97  In the PN model, a dislocation is represented as a discrete array of partial dislocations distributed on the

98  glide plane, with the balance between repulsive elastic forces and inelastic restoring forces determining

99  the shape of the dislocation. The inelastic component of the dislocation energy is parametrized here

100  using atomistic calculations of generalized stacking fault (GSF; Christian and Vítek, 1970) energies on

101  olivine slip planes, using empirical interatomic potentials to model interactions between ions. PN

102  modeling has been used to investigate glide lubrication by interstitial hydrogen atoms (Lu et al. 2001)

103  and vacant lattice sites (Lu and Kaxiras, 2002) in fcc Al, and $\{2H_{Mg}\}^X$ defects in MgO (Skelton and

104  Walker, 2018). We consider only cation vacancies on the M1 and M2 sub-lattices, represented using

105  Kröger-Vink notation (Kröger and Vink, 1956) as $\{V_{M1}\}''$ as $\{V_{M2}\}''$, such as may be created in mantle

106  olivine by oxidation of $Fe^{2+}$ to $Fe^{3+}$ at $fO_2$ or through incorporation of water under hydrous conditions.

107  **2. Methods**

108  In the PN model, a dislocations with finite core-width is represented as continuous (e.g. Joós et al.,

109  1994) or discrete (e.g. Bulatov and Kaxiras, 1997) distribution of dislocation density along the glide

110  plane. Here we use an implementation of the discrete approach previously used for modeling

111  lubrication of dislocation glide in MgO (Skelton and Walker, 2018). The total energy of such a finite

112  distribution of dislocations at a distance $R$ from the dislocation line is

113  $$E_{TOT}(R) = E_{INTERNAL} + E_{LONG-RANGED}(R) \tag{1}$$

114    where $E_{LONG\text{-}RANGED}$ is the elastic strain energy of the dislocation contained within radius $R$ and $E_{INTERNAL}$

115    is the internal energy of the dislocation distribution. This can be further decomposed as

116    $$E_{INTERNAL} = E_{ELASTIC} + E_{MISFIT} \qquad (2)$$

117    where $E_{ELASTIC}$ is the energy due to elastic interactions between the components of the dislocation

118    density and $E_{MISFIT}$ is the inelastic energy due to the lattice discontinuity across the glide plane. If $\mathbf{u}(x)$ is

119    the disregistry across the slip plane and $\rho(x) = du_i(x)/dx$ is the associated dislocation density

120    distribution, then the elastic energy of the dislocation is the work required to insert this disregistry into

121    an infinite elastic medium:

122    $$E_{ELASTIC}[\rho(x)] = -K \iint \rho(x')\rho(x)\ln|x-x'|\,dx'\,dx \quad , \qquad (3)$$

123    where $K$ is the elastic energy pre-factor, derived from the dislocation geometry and the elastic

124    constants, which are here calculated directly from the analytical derivatives of the total cell energy. In

125    the absence of a restoring force, the repelling elastic force between components of the dislocation

126    density distribution would cause the dislocation to have an infinitely wide core, with $\rho$ zero

127    everywhere. In real crystals, it is the energy penalty associated with introducing misfit on either side of

128    the slip plane that provides this opposing force, and constrains dislocations to have finite width. For a

129    given disregistry profile $\mathbf{u}(x)$, the inelastic energy is

130    $$E_{MISFIT} = \sum_n \gamma\big(u(na_p)\big)a_p \quad , \qquad (4)$$

131    where $a_p$ is the spacing between adjacent atomic planes and the function $\gamma(\mathbf{u})$ (called the $\gamma$-line in 1D)

132    gives the energy required to displace one half of a crystal by $\mathbf{u}$ (Christian and Vítek, 1970). The

133    equilibrium dislocation core structure is calculated by minimizing equation (2), under the constraint

134    that the integral of the disregistry $\mathbf{u}$ equals the Burgers vector.

135     The evolution of the disregistry profile under the action of an applied stress σ is computed by adding

136     $E_{WORK} = -\sigma \int u(x)dx$ to the total internal energy (equation 2) of the dislocation and minimizing the

137     energy functional as before. At the Peierls stress, $\sigma_p$, the energy barrier inhibiting free translation of the

138     dislocation disappears, allowing it to glide without resistance. This is equivalent to searching for the

139     stress σ at which the total energy function has no energy minimum, so that $\sigma_p$ corresponds to the

140     minimum stress for which the energy minimization step fails (Bulatov and Kaxiras, 1997).

141     The γ-surface energy used to calculate the inelastic energy of a dislocation density distribution is

142     constructed from generalized stacking fault (GSF) energies obtained from atomistic calculations. In an

143     atomistic simulation, a GSF is inserted by cutting a simulation cell with the appropriate orientation, and

144     displacing one half with respect to the other by **u**, then allowing the atomic coordinates to relax to a

145     local minimum energy configuration. For materials without rigid units, such as simple oxides, atomic

146     positions are typically constrained to relax normal to the fault plane. However, olivine contains $SiO_4$

147     polyhedra, which accommodate shear strain primarily through rotation rather than deformation. To

148     enable the $SiO_4$ tetrahedra to maintain their shape during relaxation by rotation of the whole unit, all

149     oxygen atoms are permitted to relax freely, not constrained to relax normal to the slip plane. Mg and Si

150     atoms are constrained to relax normal to the stacking fault plane. In all GSF calculations described

151     here, a 15 Å thick vacuum layer was used to minimize interactions between the GSF and its periodic

152     images. To ensure that the boundary conditions of the relaxation calculation match the bulk material,

153     the coordinates of all atoms within 5 Å of the vacuum layer were held fixed. Calculated GSF energies

154     depend on the thickness of the slab atoms used in the simulation. For stacking faults on (010), a slab

155     thickness of 8*b*, where *b* is the length of the [010] lattice vector, was found to be sufficient to converge

156     the [100](010) and [001](010) γ-line maxima to < 5 meV/Å$^2$.

157 In this study, owing to the large number of atoms in the simulation cells, atomic scale interactions are

158 modeled using empirical interatomic potentials. These potentials are taken from a widely used potential

159 model, which was parameterized by fitting to experimental data (Sanders et al., 1984; Lewis and

160 Catlow, 1985), and reproduces the physical properties of forsterite reasonably well (Price et al. 1987).

161 This potential, labeled THB1, has been widely used to model point and extended defects in forsterite,

162 including Mg point defects (Wright and Catlow, 1994), surface structures and energetics (de Leeuw et

163 al., 2000), and screw dislocation core structures and energies (Walker et al. 2005). The THB1 model

164 uses formal charges for the $Mg^{2+}$ and $Si^{4+}$ cations, while the polarizable oxygen anion is modeled as a

165 positively charged core coupled by a harmonic potential to a negatively-charged massless shell (Dick

166 and Overhauser, 1958). Each cation-anion pair interacts through a Buckingham potential, while the

167 rigidity of the $(SiO_4)^{4-}$ tetrahedron is replicated using a short-ranged three-body harmonic potential. All

168 atomistic calculations are performed using the molecular mechanics software GULP (Gale, 1997; Gale

169 and Rohl, 2003).

170 The two defect species considered in this study, $\{V_{M1}\}''$ and $\{V_{M2}\}''$, are charged, and inserting them

171 into a simulation cell gives it a net charge. This is compensated for by applying a charge-neutralizing

172 background. Creating a vacancy in the simulation cell is simple, and involves removing from the

173 simulation cell a single atom of the desired type located a specified distance from the stacking fault

174 plane. The slab thicknesses used to calculate GSF energies in the absence of Mg vacancies are

175 sufficiently great to also ensure convergence of GSF energies with point defects present at the stacking

176 fault plane. To minimize interactions between point defects and their periodic images, simulations are

177 conducted by inserting a single Mg vacancy at the slip plane of a simulation cell with cross-section

178 $2a$x$2c$, which corresponds to a concentration of 0.125 defects/site at the stacking fault plane for both

179 the M1 and M2 sub-lattices.

180 Although this would represent an unrealistically high defect concentration in the bulk lattice, the strain

181 magnitude close to a dislocation core is substantial, so that the energy of an Mg vacancy on a core site

182 may be considerably lower than in the bulk, and the defect concentration correspondingly greater. In

183 the case of MgO, fully atomistic calculations of Mg vacancy segregation to 1/2<110>{110}edge

184 dislocations give binding energies of up to 1.7 eV (Zhang et al., 2010). Concentrations of vacant sites

185 may thus be considerably greater than bulk values, potentially even approaching saturation for the

186 tightest binding sites. However, since the volumetric fraction of dislocation cores is low (<<1%), even

187 for highly deformed crystals, the concentration of vacancy related defects in the dislocation core can be

188 high without significantly changing the bulk concentration.

189 **3. Results**

190 *3.1 Point defect free forsterite*

191 In materials with complex lattices, like olivine, there may be several inequivalent planes on which slip

192 can occur. We find that the lowest energy (010) stacking fault plane is located at $z = 0.25$ (or,

193 equivalently, $z = 0.75$), intersecting the sheet of $M2O_6$ octahedra (Fig. 1a). The THB1 potential model

194 has previously been validated by Mahendran et al. (2017) at 0 GPa, who compared [100](010) and

195 [001](010) γ-lines calculated with the interatomic potential with the earlier DFT calculations by

196 Durinck et al. (2005). Although GSF energies calculated with THB1 are qualitatively consistent with

197 the DFT calculations, the energies calculated with the interatomic potential are somewhat higher,

198 particularly for displacement along [001](010). Indeed, the magnitude of the difference may actually be

199 understated, as Durinck et al. (2005) used atomic slabs only a single unit cell thick along the stacking

200 fault normal, so that their *ab initio* computed GSF energies are unlikely to be fully converged with

201 respect to slab thickness.

202 The difference between GSF energies obtained in *ab initio* and force field calculations may be due to

203 the use of formal charges in the THB1 model. The introduction of a GSF into a simulation cell often

204 brings ions at or near the stacking fault plane into close proximity with ions of like charge, so that

205 partially ionic models should in general predict lower energies than those that use formal charges. The

206 ionicity $\zeta$ of forsterite is calculated to be < 1 from refinements of electron density distributions obtained

207 using theoretical calculations (Liu et al., 2009) and synchrotron x-ray diffraction (Kirfel et al., 2005). It

208 is thus unsurprising that Durinck et al. (2005) find lower GSF energies than calculations that use the

209 THB1 potential.

210 In our calculations, we find that in point defect-free forsterite the maximum energy along the [100]

211 (010) $\gamma$-line, corresponding to the 1/2[100](010) GSF energy, increases monotonically with pressure

212 (Fig. 2). By comparison, the energy of the 1/2[001](010) GSF, which is the [001](010) $\gamma$-line

213 maximum, decreases modestly over the same pressure range. This contrasts with DFT calculations

214 (Durinck et al. 2005), which predict a pressure-independent [001](010) $\gamma$-line maximum energy,

215 although this is likely a consequence of the different simulation parameters, including simulation cell

216 size and relaxation constraints. While, at ambient pressure, the energy of the [100](010) $\gamma$-line

217 maximum is lower than that of the [001](010) $\gamma$-line maximum, the qualitatively different responses of

218 the two $\gamma$-lines to applied pressure mean that the [001](010) $\gamma$-line maximum is of lower energy above

219 ~3 GPa. The GSF energies reported here are higher than those calculated in previous studies (Durinck

220 et al., 2005; Mahendran et al., 2017), a consequence of the tighter constraints placed on the coordinates

221 of the Mg atoms during relaxation. In this study, these atoms were constrained to relax normal to the

222 stacking fault plane, whereas previous studies have permitted them to relax freely which, by increasing

223 the number of degrees of freedom to be relaxed, causes a systematic reduction in the total energy.

224 Core structures and Peierls stresses for edge and screw dislocations in forsterite were calculated using

225 the PN model (equation 2), with the inelastic energy parameterized using the $\gamma$-lines calculated in the

226 previous section. The Peierls stress calculated at ambient pressure for the [100](010) edge dislocation

227   in the point defect-free crystal is 2.4 GPa, ~25% greater than the value computed by Durinck et al.

228   (2007). The Peierls stress increases with pressure (Fig. 4), with $d\sigma_p/dP$ = 0.39, whereas the [001](010)

229   edge dislocation, $\sigma_p$ is calculated to be 3.4 GPa at ambient pressure, and has a negative pressure

230   dependence $d\sigma_p/dP$ = -0.19. The cores of [100](010) and [001](010) edge dislocations are

231   undissociated across the entire pressure range 0-10 GPa, consistent with previous PN calculations

232   (Durinck et al., 2007).

233   A screw dislocation can glide on any lattice plane containing the dislocation line vector $\xi$. Each glide

234   plane has a different structure and a correspondingly different lattice resistance, giving rise to preferred

235   glide planes. Here, we calculate the Peierls stress for [100] and [001] glide on (010), corresponding to

236   the screw dislocations that enable deformation of the [100](010) and [001](010) slip systems. The

237   Peierls stress for glide of [100] on the (010) plane at ambient pressure (Fig. 5) is 6.8 GPa, comparable

238   with the 6.3 GPa predicted by DFT-parametrized PN calculations (Durinck et al., 2007). The pressure

239   derivative is $d\sigma_p/dP$ = 0.47, somewhat greater than the pressure derivative of $d\sigma_p/dP$ = 0.39 calculated

240   by Durinck et al. (2007), but lower than the pressure derivative $d\sigma_p/dP$ ~0.67 measured in high-stress

241   deformation experiments for the average Peierls stress, which is presumably controlled by the easy

242   [100](010) slip system (Proietti et al., 2016).

243   At ambient pressure, the [001] screw dislocation glides on (010) with Peierls stress $\sigma_p$ = 5.4 GPa,

244   comparable to values calculated in previous theoretical studies, which range between 3.1 GPa (Durinck

245   et al., 2007) and 7.2 GPa (Mahendran et al., 2017). Fully atomistic calculations show that the static

246   [001] screw dislocation core has a labile non-planar structure and that the effect of applied stress is to

247   transform into a high core energy-low Peierls stress planar configuration (Carrez et al., 2008). The

248   critical stress for dislocation glide is the stress required to activate the locking-unlocking mechanism

249   for this slip system (Mahendran et al., 2017). This locking-unlocking mechanism cannot be modeled

250  within the PN formalism, and the $\sigma_p$ reported in this study is for the glissile (i.e. unlocked) dislocation

251  core gliding on the median plane of the M2O$_6$ sheet.

252  *3.2 Influence of Mg vacancies*

253  In the bulk lattice, M1 vacancies have lower energies than M2 vacancies, and are thus more abundant

254  (Brodholt, 1997). Any change in the GSF energy will depend on the interaction between the Mg

255  vacancy and the stacking fault, which can be expected to vary between the two sites. The energy of the

256  1/2[100](010) GSF with a {V$_{M1}$}″ defect adsorbed to the stacking fault plane is is 0.132 eV/Å$^2$ at 0

257  GPa, 5.7% lower than the value computed in the absence of point defects. Pressure decreases The

258  relative reduction in GSF energy by this defect (Fig. 3). {V$_{M2}$}″ defects have a more substantial impact

259  on the calculated 1/2[100](010) GSF energy, reducing calculated GSF energies by 13.6 % to 0.121

260  eV/Å$^2$ at ambient pressure, although the relative reduction again decreases with pressure. Calculated

261  1/2[001](010) GSF energies are marginally increased by the adsoprtion of {V$_{M1}$}″ defects to the fault

262  plane. The 1/2[001](010) GSF energy calculated with a {V$_{M1}$}″ defect at the fault plane is 0.168 eV/Å$^2$

263  at ambient pressure, decreasing to 0.145 eV/Å$^2$ at 10 GPa, slightly higher than the corresponding values

264  for the point defect free GSF. {V$_{M2}$}″ defects reduce the 1/2[001](010) GSF energy by ~ 22 % to 0.127

265  eV/Å$^2$. At 10 GPa, the energy of this GSF is 0.101 eV/Å$^2$, corresponding to a -28.9% change in the

266  GSF energy relative to the point defect-free GSF case. {V$_{M2}$}″ in the sheet of M2O$_6$ octahedra not

267  located at the glide plane have no discernible impact on the stacking fault energy.

268  For [100](010) edge dislocations, the adsorption of a {V$_{M1}$}″ defect to the stacking fault plane reduces

269  the Peierls stress by -16% at ambient pressure, to 2.0 GPa, but the pressure dependence of $\sigma_p$ is not

270  significantly changed by the presence of this defect. The effect of the {V$_{M2}$}″ defect is more substantial,

271  and for this defect $\sigma_p$ = 1.2 GPa at ambient pressure, slightly more than half the Peierls stress calculated

272  for a dislocation without adsorbed vacancies. Moreover, unlike the {V$_{M1}$}″ defect, {V$_{M2}$}″ defects

273  reduce the pressure sensitivity of this slip system, giving d$\sigma_p$/d$P$ = 0.31. The [001](010) edge

274 dislocation responds quite differently from [100](010) edge dislocation to the presence of Mg

275 vacancies (Fig. 4). The Peierls stress is increased by the presence of $\{V_{M1}\}''$ defects. The Peierls stress

276 decreases with pressure at a rate $d\sigma_p/dP$ = -0.10, almost a factor of 2 smaller in magnitude than

277 calculated in the absence of point defects. The Peierls stress of the [001](010) edge dislocation is

278 considerably reduced by $\{V_{M2}\}''$ defects, to 1.6 GPa at ambient pressure, and decreases with pressure

279 (Fig. 4c).

280 For [100](010) screw dislocations (Fig. 5), the presence of Mg vacancies at the glide plane reduces the

281 Peierls stress. If the Mg vacancy is located on an M2 site, $\sigma_p$ is calculated to be 6.1 GPa, 10.2% lower

282 than in point defect-free forsterite, and increases with pressure to 10.7 GPa at 10 GPa. The pressure

283 sensitivity of the [100] screw dislocation is unaffected by $\{V_{M1}\}''$ defects as $d\sigma_p/dP$ = 0.46, nearly

284 identical to the value found previously for this dislocation in the absence of adsorbed vacancies. For an

285 Mg vacancy located on an M1 site close to (but not on) the slip plane, calculated values for $\sigma_p$ at these

286 pressures are comparable, 6.3 GPa and 10.8 GPa at 0 and 10 GPa, respectively, as is the pressure

287 derivative $d\sigma_p/dP$, which is 0.45. The Peierls stresses of [001] screw dislocations gliding on (010) are

288 similarly reduced by the presence of $\{V_{M2}\}''$ defects (Fig. 5), but the pressure derivative $d\sigma_p/dP$ is

289 unchanged. The relative Peierls stress reduction induced by the presence of M2 vacancies actually

290 increases with pressure, from -44% at ambient pressure to -75% at 10 GPa. Just as in the case of [001]

291 (010) edge dislocations, glide of [001] screw dislocations on (010) is modestly inhibited by the

292 presence of M1 vacancies, and the magnitude of $d\sigma_p/dP$ is reduced, relative to the point defect-free

293 value.

294 The markedly different sensitivities of the [100](010) and [001](010) $\gamma$-lines to adsorption of $\{V_{M1}\}''$

295 versus $\{V_{M2}\}''$ defects to the stacking fault, and thus on the Peierls stresses of the associated

296 dislocations, is a direct consequence of the location of the slip plane in the unit cell. As the lowest

297  energy slip plane lies across the center of the sheet of $M2O_6$ octahedra that is parallel to the (010)

298  plane, it does not intersect $M1O_6$ octahedra or $SiO_4$ tetrahedra (Fig. 1a), so that the creation of M1

299  vacancies cannot contribute to the total number of vacant lattice sites at the slip plane. The lubrication

300  effect is greatest for [001](010) γ-line energies, as the minimum distance between M2 sites across the

301  fault plane is 2.61 Å (at the γ-line maximum), compared with 3.89 Å for the [100](010) γ-line. As the

302  $\{V_{M2}\}''$ defect interacts more strongly than the $\{V_{M1}\}''$ defect with both 1/2[100](010) and [001](010)

303  stacking faults, $\{V_{M2}\}''$ defects can be expected to be relatively more abundant near the dislocation core

304  than in the bulk lattice.

305  Nevertheless, $\{V_{M1}\}''$ defects do still reduce the energy of the [100](010) γ-line, although [001](010) γ-

306  line energies are essentially unchanged. This is because displacement of the upper half the simulation

307  cell by 1/2[100] brings M2 and Si sites on opposite sites of the stacking plane into close proximity.

308  Relaxing the atom in the M2 site away from the stacking fault reduces the energy of the slab, which is

309  easier when a void has been created above the M2 site by the insertion of a $\{V_{M1}\}''$ defect. At 0 GPa,

310  this increases the relaxed M2-Si distance from 2.939 Å to 3.021 Å. Furthermore, a sub-periodic

311  modulation of the M1 site coordinates is introduced, as the Mg atoms in the layer of M1 sites closest to

312  the GSF stacking fault are displaced ~0.2 Å along the fault plane normal. The sign of the displacement

313  vector alternates along [001]. For the olivine crystal structure, [001](010) slip does not cause cations to

314  approach as closely as does [100](010) slip, and there is thus less potential for vacant cation sites away

315  from the slip plane to reduce GSF energies by accommodating relaxation away from the stacking fault.

316  Adsorbed vacancies can also alter the core width ξ. For example $\{V_{M2}\}''$ defects increase the half-width

317  ξ of [001](010) edge dislocations from 4.6 Å to 5.8 Å at 0 GPa, and 4.6 Å to 6.2 Å at 10 GPa pressure.

318  The half-width of [001] screw dislocations is likewise increased, from 2.9 Å to 3.4 Å at ambient

319  pressure. This is consistent with the established relationship between ξ and $\sigma_p$, with increases in the

320  former causing reduction of the latter. The influence of M2 vacancies on the width of [100](010) edge

321   and [100] screw dislocations, for which smaller Peierls stress reductions are predicted, is comparatively

322   small. At ambient pressure, $\xi$ increases from 2.2 Å to 2.3 Å for edge dislocations, and from 1.8 Å to 2.0

323   Å for screw dislocations. M1 vacancies have have a limited effect on the shapes of [100](010) edge

324   dislocations, and only marginally increase the half-width of [100] screw dislocations. However, M1

325   vacancies reduce the widths of [001](010) edge dislocations and [001] screw dislocation, to 4.3 Å and

326   2.3 Å at ambient pressure, respectively. Broadening of the dislocation core provides a plausible

327   mechanism by which vacancies may enhance dislocation glide, a point that could be clarified in the

328   future using fully atomistic simulations of point defect-dislocation interactions.

329   **4. Discussion**

330   In vacancy-free forsterite, the ratio $\sigma_{p,[100]}/\sigma_{p,[001]}$ increases with $P$ for both the edge and screw

331   components of both slip systems. For edge dislocations, $\sigma_{p,[100]}/\sigma_{p,[001]}$ varies from 0.71 at ambient

332   pressure, to 4.4 at 10 GPa (Fig. 6a). The addition of $\{V_{M1}\}''$ vacancies changes this ratio, decreasing it

333   to 0.54 at ambient pressure and reducing the pressure sensitivity so that, at 10 GPa, it is just 2.16. In

334   contrast, $\{V_{M2}\}''$ defects increase the ratio, to 0.77 at 0 GPa and 28.51 at 10 GPa. In each case, the ratio

335   $\sigma_{p,[100]}/\sigma_{p,[001]} = 1$ corresponds to the pressure at which [100](010) glide becomes harder than [001](010)

336   glide. This occurs at 1.5 GPa with no point defects present, increasing to 3.6 GPa when $\{V_{M1}\}''$ defects

337   are adsorbed to the stacking fault and decreases to 0.7 GPa upon adsorption of $\{V_{M2}\}''$ defects to the

338   stacking fault plane. In the case of screw dislocations, $\sigma_{p,[100]}/\sigma_{p,[001]}$ is strictly > 1. However, $\{V_{M1}\}''$

339   defects reduce it from 1.26 to 1.09 at ambient pressure, and from 3.49 to 2.50 at 10 GPa. The $\{V_{M2}\}''$

340   defect has the reverse effect on the two slip systems, increasing $\sigma_{p,[100]}/\sigma_{p,[001]}$ to 2.06 at ambient pressure

341   and 13.10 and 10 GPa. From this, we conclude that, while $\{V_{M1}\}''$ defects cause the relative activities

342   of the two slip systems to converge at constant $P$, $\{V_{M2}\}''$ defects enhance slip on [001](010).

343 As qualitatively predicted by our models, experimental studies have reported a pressure-induced

344 change in the deformation fabric of anhydrous olivine, caused by a change of the preferred slip system

345 from [100](010) to [001](010) (Couvy et al., 2004; Raterron et al., 2016). This transition may be

346 observable in seismological models for the Earth's upper mantle. The LPO of Fe-bearing $Fo_{90}$ olivine

347 suggests a change from dominant [100](010) to [001](010) slip at ~3 GPa, which corresponds to a

348 mantle depth of approximately 70-80 km (Jung et al., 2009). At 0 GPa, the [100](010) edge dislocation

349 has the lowest Peierls stress and so should be the dominant slip system during glide deformation.

350 However, because pressure is calculated to suppress the activity of this slip system, the Peierls stress of

351 the [001](010) edge dislocation is lower at high pressure. The $P$-$\sigma_p$ curves of the two slip systems in

352 point defect-free forsterite intersect at 1.5 GPa (Fig. 4a), slightly lower than the pressures reported in

353 experiments.

354 Deformation experiments produce different olivine textures under dry and wet conditions. One

355 plausible reason for this is that hydrated vacancies lubricate [001](010) glide more than [100](010)

356 glide (Katayama et al. 2004), leading to the development of the flow normal B-type fabric associated

357 with the mantle wedge. Ohuchi et al. (2012) have found that the transition between the two fabrics

358 occurs at ~650 ppm H/Si.  Consistent with this, we find that the Peierls stresses of [100](010) edge and

359 screw dislocations are reduced less by the presence of M-site vacancies than [001](010) edge and screw

360 dislocations. Realistic vacancy-related defect concentrations are insufficient to change the weakest slip

361 system at ambient pressure. However, the differential effect on the Peierls stresses of the [100](010)

362 and [001](010) edge dislocations is enough to reduce the pressure at which the Peierls stresses of the

363 two slip systems cross over. When the inelastic restoring force is parametrized using the γ-lines

364 calculated with vacancies adsorbed to the slip plane, $P_{\text{cross-over}}$ decreases from 1.5 GPa to 0.7 GPa.

365 Higher defect concentrations at the dislocation core will cause the slip system cross-over to be

366 displaced to even lower pressures. Similarly, differences between concentrations of vacancy-related

367 defects at the glide planes of the two slip systems will displace the cross-over pressure. Increasing the

368 concentration $\{V_{M2}\}''$ defects adsorbed to the [100](010) dislocation or decreasing the concentration of

369 defects adsorbed to the [001](010) dislocation will reduce $P_{cross-over}$. Changing either of the

370 concentrations in the opposite direction increases $P_{cross-over}$.

371 The calculated influence of vacancy-related defects on the Peierls stress of olivine may be of

372 significance for development of LPO during deformation. It has also been suggested that a distinct LPO

373 may form in olivine when it is deformed via diffusion creep (Miyazaki et al., 2013). Similarly, a

374 transition to a grain boundary sliding deformation mechanism may explain the presence of the B-type

375 deformation fabric, rather than water-induced changes to the relative strengths of olivine slip systems.

376 However, as these calculations show, the adsorption of vacancies, and by implication vacancy-related

377 defects, is sufficient to induce a change in the deformation fabric of olivine similar to that observed by

378 Katayama and Karato (2008) under hydrous conditions. In tomographic images of shear wave

379 anisotropy, this might show up as a reduction of the depth at which the deformation fabric changes

380 from A-type (i.e. [100](010)) to B-type (i.e. [001](010)). Alternatively, if water is present only at

381 shallow depths, the shear wave anisotropy may match the B-type fabric at shallow depths, transitioning

382 to the A-type deformation fabric as the modal abundance of water decreases. The B-type deformation

383 fabric then re-emerges at high pressure as the relative activity of the [001](010) slip system increases.

384 These conclusions carry over to the dislocation-accommodated grain-boundary sliding regime. This

385 deformation mechanism leads to the development of a pronounced LPO that relates to the slip system

386 accommodating grain boundary sliding (Hansen et al., 2011; Hansen et al., 2012ab), which will be

387 altered by the presence of hydrous vacancies.

388 Incorporation of water is not the only mechanism by which vacancies can be generated in olivine

389 minerals. Trivalent cations such as $Al^{3+}$, $Sc^{3+}$ and $Fe^{3+}$ can substitute for $Mg^{2+}$ (or $Fe^{2+}$) in the olivine

390  lattice, charge-balanced either the replacement of $Si^{4+}$ by a trivalent cation or, more commonly, the

391  creation of M-site vacancies (Colson et al., 1989). The latter substitution mechanism can be written as

392  $$3\cdot\left[M_M^{2+}\right]^X + M_2^{3+}O_3 \rightleftharpoons 2\cdot\left[M_M^{3+}\right]^\cdot + \left[V_M\right]'' + 3\cdot M^{2+}O \quad , \tag{5}$$
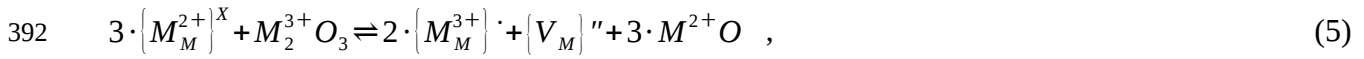
393  where $M^{2+}$ is typically $Mg^{2+}$ or, in iron-bearing olivine, $Fe^{2+}$ and $M^{3+}$ is the substituting trivalent cation.

394  These vacancies can influence the mechanical properties of olivine, for instance by enhancing seismic

395  attenuation due to grain boundary mechanisms (Cline et al., 2018). The solubility of common trivalent

396  elements in olivine is sufficiently high that vacancies created by the substitution reaction (5) can greatly

397  outnumber intrinsic vacancies, such as those associated with Schottky defects (van Orman et al., 2009).

398  In $(Mg,Fe)_2SiO_4$, M-site vacancies are produced by oxidation of iron from $Fe^{2+}$ to $Fe^{3+}$, and at high $fO_2$

399  $\{Fe^{3+}_M\}^\cdot$ and $\{V_M\}''$ are the most abundant defects (Stocker, 1978). These defects may be unassociated

400  at high temperature and pressure, as they are in the common oxide $(Mg,Fe)O$ (Otsuka et al., 2010), and

401  we expect such vacancies to alter the Peierls stress of dislocations in olivine.

402  **5. Conclusions**

403  In this study, we used atomistic calculations of generalized stacking fault energies in forsterite, the Mg

404  end-member of olivine, to parameterize Peierls-Nabarro models of pure edge and screw dislocation. To

405  probe the possible influence of vacancy-related defects on the Peierls stress, energies were calculated

406  for GSFs in point defect-free forsterite, and with $\{V_{M1}\}''$ and $\{V_{M2}\}''$ defects segregated to lattice sites

407  in close proximity to the stacking fault plane. It was found that vacancies are capable of reducing $\gamma$-line

408  energies and, correspondingly, Peierls stresses for many of the major slip systems in olivine. However,

409  the magnitude of this decrease depends strongly on both the slip system and the site on which the

410  vacancy is located. $\{V_{M2}\}''$ defects at lattice sites adjacent to the glide plane have the greatest effect on

411  the Peierls stress of both slip systems, while the magnitude of the $\sigma_p$ reduction is greatest for the [001]

412     (010) slip system. In the case of edge dislocations, this reduces the pressure at which the hardening of

413     [100](010) glide cause [001](010) to become the dominant slip system.

414     Cation vacancies in olivine are associated with intrinsic defect mechanisms (Schottky and Frenkel

415     defects). However, in natural olivine, vacancy concentrations are, in most cases, probably controlled by

416     extrinsic defect mechanisms, such as the creation of protonated vacancies in hydrated systems, the

417     oxidation of $Fe^{2+}$ to $Fe^{3+}$, or the charge-balanced substitution of heterovalent impurities, such $Al^{3+}$ or

418     $Cr^{3+}$. Each of these mechanisms will be operative in at least some regions of the Earth's upper mantle.

419     Hydration and oxidation are especially relevant in mantle wedges above subduction zones. There,

420     concentrations of vacancy related defects are likely to be elevated, due to the combination of oxidizing

421     conditions and the availability of liquid water from dehydrating phases in the subducting slab. Our

422     models suggest that such point defects can reduce the Peierls stress of dislocations in olivine in mantle

423     wedges, potentially linking crystal chemistry to the observed variations in seismic anisotropy in these

424     regions.

433     **References**

434   [1] Bai, Q., Kohlstedt, D.L., 1993. Effects of chemical environment on the solubility and incorporation
435   mechanism for hydrogen in olivine. Phys Chem Minerals 19, 460–471.
436   https://doi.org/10.1007/BF00203186

437   [2] Berry, A.J., Hermann, J., O'Neill, H.S.C., Foran, G.J., 2005. Fingerprinting the water site in mantle
438   olivine. Geology 33, 869–872. https://doi.org/10.1130/G21759.1

439   [3] Braithwaite, J.S., Sushko, P.V., Wright, K., Catlow, C.R.A., 2002. Hydrogen defects in Forsterite: A
440   test case for the embedded cluster method. The Journal of Chemical Physics 116, 2628–2635.
441   https://doi.org/10.1063/1.1433465

442   [4] Brodholt, J., 1997. Ab initio calculations on point defects in forsterite (Mg2SiO4) and implications
443   for diffusion and creep. American Mineralogist 82, 1049–1053. https://doi.org/10.2138/am-1997-11-
444   1201

445   [5] Christian, J.W., Vítek, V., 1970. Dislocations and stacking faults. Rep. Prog. Phys. 33, 307.
446   https://doi.org/10.1088/0034-4885/33/1/307

447   [6] Bulatov, V.V., Kaxiras, E., 1997. Semidiscrete Variational Peierls Framework for Dislocation Core
448   Properties. Phys. Rev. Lett. 78, 4221–4224. https://doi.org/10.1103/PhysRevLett.78.4221

449   [7] Carrez, P., Walker, A.M., Metsue, A., Cordier, P., 2008. Evidence from numerical modelling for 3D
450   spreading of [001] screw dislocations in Mg2SiO4 forsterite. Philosophical Magazine 88, 2477–2485.
451   https://doi.org/10.1080/14786430802363804

452   [8] Cline II, C.J., Faul, U.H., David, E.C., Berry, A.J., Jackson, I., 2018. Redox-influenced seismic
453   properties of upper-mantle olivine. Nature 555, 355–358. https://doi.org/10.1038/nature25764

454   [9] Colson, R.O., McKay, G.A., Taylor, L.A., 1989. Charge balancing of trivalent trace elements in
455   olivine and low-Ca pyroxene: A test using experimental partitioning data. Geochimica et
456   Cosmochimica Acta 53, 643–648. https://doi.org/10.1016/0016-7037(89)90007-0

457   [10] Cottrell, A.H., Bilby, B.A., 1949. Dislocation Theory of Yielding and Strain Ageing of Iron. Proc.
458   Phys. Soc. A 62, 49. https://doi.org/10.1088/0370-1298/62/1/308

459   [11] Couvy, H., Frost, D.J., Heidelbach, F., Nyilas, K., Ungár, T., Mackwell, S., Cordier, P., 2004. Shear
460   deformation experiments of forsterite at 11 GPa - 1400°C in the multianvil apparatus. European Journal
461   of Mineralogy 16, 877–889. https://doi.org/10.1127/0935-1221/2004/0016-0877

462   [12] Demouchy, S., Tommasi, A., Boffa Ballaran, T., Cordier, P., 2013. Low strength of Earth's
463   uppermost mantle inferred from tri-axial deformation experiments on dry olivine crystals. Physics of
464   the Earth and Planetary Interiors 220, 37–49. https://doi.org/10.1016/j.pepi.2013.04.008

465   [13] Dick, B.G., Overhauser, A.W., 1958. Theory of the Dielectric Constants of Alkali Halide Crystals.
466   Phys. Rev. 112, 90–103. https://doi.org/10.1103/PhysRev.112.90

467 [14] Durinck, J., Legris, A., Cordier, P., 2005. Pressure sensitivity of olivine slip systems: first-principle
468 calculations of generalised stacking faults. Phys Chem Minerals 32, 646–654.
469 https://doi.org/10.1007/s00269-005-0041-2

470 [15] Durinck, J., Carrez, P., Cordier, P., 2007. Application of the Peierls-Nabarro model to dislocations
471 in forsterite. European Journal of Mineralogy 19, 631–639. https://doi.org/10.1127/0935-
472 1221/2007/0019-1757

473 [16] Evans, B., Goetze, C., 1979. The temperature variation of hardness of olivine and its implication
474 for polycrystalline yield stress. J. Geophys. Res. 84, 5505–5524.
475 https://doi.org/10.1029/JB084iB10p05505

476 [17] Faul, U.H., Cline II, C.J., David, E.C., Berry, A.J., Jackson, I., 2016. Titanium-hydroxyl defect-
477 controlled rheology of the Earth's upper mantle. Earth and Planetary Science Letters 452, 227–237.
478 https://doi.org/10.1016/j.epsl.2016.07.016

479 [18] Faul, U.H., Ii, C.J.C., Berry, A., Jackson, I., Garapić, G., 2017. Constraints on oxygen fugacity
480 within metal capsules. Phys Chem Minerals 1–13. https://doi.org/10.1007/s00269-017-0937-7

481 [19] Gale, J.D., 1997. GULP: A computer program for the symmetry-adapted simulation of solids. J.
482 Chem. Soc., Faraday Trans. 93, 629–637. https://doi.org/10.1039/A606455H

483 [20] Gale, J.D., Rohl, A.L., 2003. The General Utility Lattice Program (GULP). Molecular Simulation
484 29, 291–341. https://doi.org/10.1080/0892702031000104887

485 [21] Goetze, C., Kohlstedt, D.L., 1973. Laboratory study of dislocation climb and diffusion in olivine.
486 J. Geophys. Res. 78, 5961–5971. https://doi.org/10.1029/JB078i026p05961

487 [22] Hansen, L.N., Zimmerman, M.E., Kohlstedt, D.L., 2011. Grain boundary sliding in San Carlos
488 olivine: Flow law parameters and crystallographic-preferred orientation. J. Geophys. Res. 116, B08201.
489 https://doi.org/10.1029/2011JB008220

490 [23] Hansen, L.N., Zimmerman, M.E., Kohlstedt, D.L., 2012a. The influence of microstructure on
491 deformation of olivine in the grain-boundary sliding regime. J. Geophys. Res. 117, B09201.
492 https://doi.org/10.1029/2012JB009305

493 [24] Hansen, L.N., Zimmerman, M.E., Kohlstedt, D.L., 2012b. Laboratory measurements of the
494 viscous anisotropy of olivine aggregates. Nature 492, 415. https://doi.org/10.1038/nature11671

495 [25] Hilairet, N., Wang, Y., Sanehira, T., Merkel, S., Mei, S., 2012. Deformation of olivine under
496 mantle conditions: An in situ high-pressure, high-temperature study using monochromatic synchrotron
497 radiation. J. Geophys. Res. 117, B01203. https://doi.org/10.1029/2011JB008498

498 [26] Idrissi, H., Bollinger, C., Boioli, F., Schryvers, D., Cordier, P., 2016. Low-temperature plasticity of
499 olivine revisited with in situ TEM nanomechanical testing. Science Advances 2, e1501671.
500 https://doi.org/10.1126/sciadv.1501671

501 [27] Jackson, I., Faul, U.H., Skelton, R., 2014. Elastically accommodated grain-boundary sliding: New
502 insights from experiment and modeling. Physics of the Earth and Planetary Interiors, High-Pressure
503 Research in Earth Science: Crust, Mantle, and Core 228, 203–210.
504 https://doi.org/10.1016/j.pepi.2013.11.014

505 [28] Joós, B., Ren, Q., Duesbery, M.S., 1994. Peierls-Nabarro model of dislocations in silicon with
506 generalized stacking-fault restoring forces. Phys. Rev. B 50, 5890–5898.
507 https://doi.org/10.1103/PhysRevB.50.5890

508 [29] Jung, H., Karato, S., 2001. Water-Induced Fabric Transitions in Olivine. Science 293, 1460–1463.
509 https://doi.org/10.1126/science.1062235

510 [30] Jung, H., Katayama, I., Jiang, Z., Hiraga, T., Karato, S., 2006. Effect of water and stress on the
511 lattice-preferred orientation of olivine. Tectonophysics 421, 1–22.
512 https://doi.org/10.1016/j.tecto.2006.02.011

513 [31] Jung, H., Mo, W., Green, H.W., 2009. Upper mantle seismic anisotropy resulting from pressure-
514 induced slip transition inolivine. Nature Geosci 2, 73–77. https://doi.org/10.1038/ngeo389

515 [32] Katayama, I., Karato, S., 2008. Low-temperature, high-stress deformation of olivine under water-
516 saturated conditions. Physics of the Earth and Planetary Interiors 168, 125–133.
517 https://doi.org/10.1016/j.pepi.2008.05.019

518 [33] Katayama, I., Jung, H., Karato, S., 2004. New type of olivine fabric from deformation experiments
519 at modest water content and low stress. Geology 32, 1045–1048. https://doi.org/10.1130/G20805.1

520 [34] Katayama, I., Karato, S., Brandon, M., 2005. Evidence of high water content in the deep upper
521 mantle inferred from deformation microstructures. Geology 33, 613–616.
522 https://doi.org/10.1130/G21332.1

523 [35] Kelley, K.A., Cottrell, E., 2009. Water and the Oxidation State of Subduction Zone Magmas.
524 Science 325, 605–607. https://doi.org/10.1126/science.1174156

525 [36] Kirfel, A., Lippmann, T., Blaha, P., Schwarz, K., Cox, D.F., Rosso, K.M., Gibbs, G.V., 2005.
526 Electron density distribution and bond critical point properties for forsterite, Mg2 SiO4, determined
527 with synchrotron single crystal X-ray diffraction data. Phys Chem Minerals 32, 301–313.
528 https://doi.org/10.1007/s00269-005-0468-5

529 [37] Kohlstedt, D.L., Keppler, H., Rubie, D.C., 1996. Solubility of water in the α, β and γ phases of
530 (Mg,Fe)2SiO4. Contrib Mineral Petrol 123, 345–357. https://doi.org/10.1007/s004100050161

531  [38] Kranjc, K., Rouse, Z., Flores, K.M., Skemer, P., 2016. Low-temperature plastic rheology of olivine

532  determined by nanoindentation. Geophys. Res. Lett. 43, 2015GL065837.

533  https://doi.org/10.1002/2015GL065837

534  [39] Kröger, F.A., Vink, H.J., 1956. Relations between the Concentrations of Imperfections in

535  Crystalline Solids. Solid State Physics 3, 307–435. https://doi.org/10.1016/S0081-1947(08)60135-6

536  [40] de Leeuw, N.H., Parker, S.C., Catlow, C.R.A., Price, G.D., 2000. Modelling the effect of water on

537  the surface structure and stability of forsterite. Phys Chem Min 27, 332–341.

538  https://doi.org/10.1007/s002690050262

539  [41] Lemaire, C., Kohn, S.C., Brooker, R.A., 2004. The effect of silica activity on the incorporation

540  mechanisms of water in synthetic forsterite: a polarised infrared spectroscopic study. Contrib Mineral

541  Petrol 147, 48–57. https://doi.org/10.1007/s00410-003-0539-x

542  [42] Lewis, G.V., Catlow, C.R.A., 1985. Potential models for ionic oxides. J. Phys. C: Solid State Phys.

543  18, 1149. https://doi.org/10.1088/0022-3719/18/6/010

544  [43] Liu, L., Du, J., Zhao, J., Liu, H., Gao, H., Chen, Y., 2009. Elastic properties of hydrous forsterites

545  under high pressure: First-principle calculations. Physics of the Earth and Planetary Interiors 176, 89–

546  97. https://doi.org/10.1016/j.pepi.2009.04.004

547  [44] Long, M.D., Becker, T.W., 2010. Mantle dynamics and seismic anisotropy. Earth and Planetary

548  Science Letters 297, 341–354. https://doi.org/10.1016/j.epsl.2010.06.036

549  [45] Long, M.D., Silver, P.G., 2009. Shear Wave Splitting and Mantle Anisotropy: Measurements,

550  Interpretations, and New Directions. Surv Geophys 30, 407–461. https://doi.org/10.1007/s10712-009-

551  9075-1

552  [46] Lu, G., Kaxiras, E., 2002. Can Vacancies Lubricate Dislocation Motion in Aluminum? Phys. Rev.

553  Lett. 89, 105501. https://doi.org/10.1103/PhysRevLett.89.105501

554  [47] Lu, G., Zhang, Q., Kioussis, N., Kaxiras, E., 2001. Hydrogen-Enhanced Local Plasticity in

555  Aluminum: An Ab Initio Study. Phys. Rev. Lett. 87, 095501.

556  https://doi.org/10.1103/PhysRevLett.87.095501

557  [48] Mahendran, S., Carrez, P., Groh, S., Cordier, P., 2017. Dislocation modelling in Mg 2 SiO 4

558  forsterite: an atomic-scale study based on the THB1 potential. Modelling Simul. Mater. Sci. Eng. 25,

559  054002. https://doi.org/10.1088/1361-651X/aa6efa

560  [49] Mainprice, D., 2007. Seismic Anisotropy of the Deep Earth from a Mineral and Rock Physics

561  Perspective, in: Treatise of Geophysics, Vol.2. Elsevier, pp. 437–491.

562 [50] Mainprice, D., Tommasi, A., Couvy, H., Cordier, P., Frost, D.J., 2005. Pressure sensitivity of

563 olivine slip systems and seismic anisotropy of Earth's upper mantle. Nature 433, 731.

564 https://doi.org/10.1038/nature03266

565 [51] Margheriti, L., Nostro, C., Cocco, M., Amato, A., 1996. Seismic anisotropy beneath the Northern

566 Apennines (Italy) and its tectonic implications. Geophys. Res. Lett. 23, 2721–2724.

567 https://doi.org/10.1029/96GL02519

568 [52] Martin, R.F., Donnay, G., 1972. Hydroxyl in the mantle. American Mineralogist 57, 554–570.

569 [53] Miyazaki, T., Sueyoshi, K., Hiraga, T., 2013. Olivine crystals align during diffusion creep of

570 Earth/'s upper mantle. Nature 502, 321–326. https://doi.org/10.1038/nature12570

571 [54] Mizukami, T., Wallis, S.R., Yamamoto, J., 2004. Natural examples of olivine lattice preferred

572 orientation patterns with a flow-normal a-axis maximum. Nature 427, 432–436.

573 https://doi.org/10.1038/nature02179

574 [55] Mei, S., Kohlstedt, D.L., 2000. Influence of water on plastic deformation of olivine aggregates: 1.

575 Diffusion creep regime. J. Geophys. Res. 105, 21457–21469. https://doi.org/10.1029/2000JB900179

576 [56] Nabarro, F.R.N., 1947. Dislocations in a simple cubic lattice. Proc. Phys. Soc. 59, 256.

577 https://doi.org/10.1088/0959-5309/59/2/309

578 [57] Nicolas, A., Christensen, N.I., 1987. Formation of Anisotropy in Upper Mantle Peridotites - A

579 Review, in: Fuchs, K., Froidevaux, C. (Eds.), Composition, Structure and Dynamics of the Lithosphere-

580 Asthenosphere System. American Geophysical Union, pp. 111–123.

581 https://doi.org/10.1029/GD016p0111

582 [58] Ohuchi, T., Kawazoe, T., Nishihara, Y., Nishiyama, N., Irifune, T., 2011. High pressure and

583 temperature fabric transitions in olivine and variations in upper mantle seismic anisotropy. Earth and

584 Planetary Science Letters 304, 55–63. https://doi.org/10.1016/j.epsl.2011.01.015

585 [59] Ohuchi, T., Kawazoe, T., Nishihara, Y., Irifune, T., 2012. Change of olivine a-axis alignment

586 induced by water: Origin of seismic anisotropy in subduction zones. Earth and Planetary Science

587 Letters 317–318, 111–119. https://doi.org/10.1016/j.epsl.2011.11.022

588 [60] van Orman, J.A., Fei, Y., Hauri, E.H., Wang, J., 2003. Diffusion in MgO at high pressures:

589 Constraints on deformation mechanisms and chemical transport at the core-mantle boundary. Geophys.

590 Res. Lett. 30, 1056. https://doi.org/10.1029/2002GL016343

591 [61] Otsuka, K., McCammon, C.A., Karato, S., 2010. Tetrahedral occupancy of ferric iron in

592 (Mg,Fe)O: Implications for point defects in the Earth's lower mantle. Physics of the Earth and

593 Planetary Interiors, Transport properties of the lower mantle 180, 179–188.

594 https://doi.org/10.1016/j.pepi.2009.10.005

595 [62] Peierls, R., 1940. The size of a dislocation. Proc. Phys. Soc. 52, 34. https://doi.org/10.1088/0959-
596 5309/52/1/305

597 [63] Price, G.D., Parker, S.C., Leslie, M., 1987. The lattice dynamics and thermodynamics of the
598 Mg2SiO4 polymorphs. Phys Chem Minerals 15, 181–190. https://doi.org/10.1007/BF00308782

599 [64] Proietti, A., Bystricky, M., Guignard, J., Béjina, F., Crichton, W., 2016. Effect of pressure on the
600 strength of olivine at room temperature. Physics of the Earth and Planetary Interiors 259, 34–44.
601 https://doi.org/10.1016/j.pepi.2016.08.004

602 [65] Raterron, P., Chen, J., Geenen, T., Girard, J., 2011. Pressure effect on forsterite dislocation slip
603 systems: Implications for upper-mantle LPO and low viscosity zone. Physics of the Earth and Planetary
604 Interiors 188, 26–36. https://doi.org/10.1016/j.pepi.2011.06.009

605 [66] Raterron, P., Chen, J., Li, L., Weidner, D., Cordier, P., 2016. Pressure-induced slip-system
606 transition in forsterite: Single-crystal rheological properties at mantle pressure and temperature.
607 American Mineralogist 92, 1436–1445. https://doi.org/10.2138/am.2007.2474

608 [67] Sanders, M.J., Leslie, M., Catlow, C.R.A., 1984. Interatomic potentials for SiO2. J. Chem. Soc.,
609 Chem. Commun. 1271–1273. https://doi.org/10.1039/C39840001271

610 [68] Skelton, R., Walker, A.M., 2018. Lubrication of dislocation glide in MgO by hydrous defects. Phys
611 Chem Minerals 1–14. https://doi.org/10.1007/s00269-018-0957-y

612 [69] Smith, G.P., Wiens, D.A., Fischer, K.M., Dorman, L.M., Webb, S.C., Hildebrand, J.A., 2001. A
613 Complex Pattern of Mantle Flow in the Lau Backarc. Science 292, 713–716.
614 https://doi.org/10.1126/science.1058763

615 [70] Stocker, R.L., 1978. Influence of oxygen pressure on defect concentrations in olivine with a fixed
616 cationic ratio. Physics of the Earth and Planetary Interiors 17, 118–129. https://doi.org/10.1016/0031-
617 9201(78)90053-5

618 [71] Walker, A.M., Gale, J.D., Slater, B., Wright, K., 2005. Atomic scale modelling of the cores of
619 dislocations in complex materials part 2: applications. Phys. Chem. Chem. Phys. 7, 3235–3242.
620 https://doi.org/10.1039/B505716G

621 [72] Walker, A.M., Hermann, J., Berry, A.J., O'Neill, H.S.C., 2007. Three water sites in upper mantle
622 olivine and the role of titanium in the water weakening mechanism. J. Geophys. Res. 112, B05211.
623 https://doi.org/10.1029/2006JB004620

624 [73] Wright, K., Catlow, C.R.A., 1994. A computer simulation study of (OH) defects in olivine. Phys
625 Chem Minerals 20, 515–518. https://doi.org/10.1007/BF00203222

626   [74] Zhang, F., Walker, A.M., Wright, K., Gale, J.D., 2010. Defects and dislocations in MgO: atomic

627   scale models of impurity segregation and fast pipe diffusion. J. Mater. Chem. 20, 10445–10451.

628   https://doi.org/10.1039/C0JM01550D

629   **Figure captions**
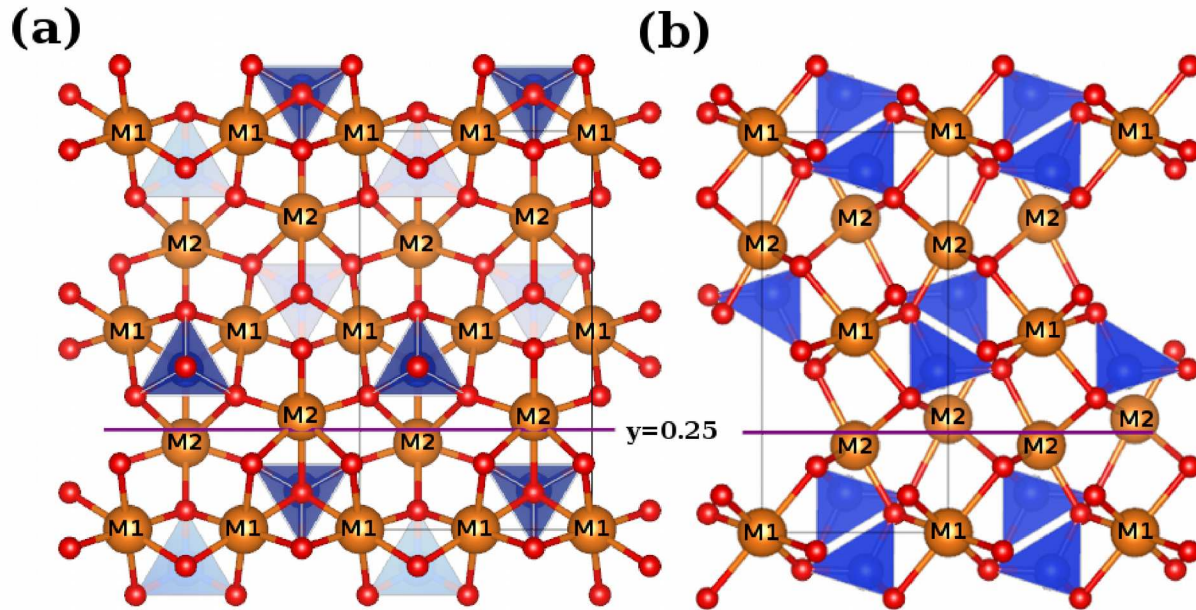


630

631   **Fig. 1** The olivine unit cell, viewed down the (a) [100] and (b) [001] cell directions, with the M1 and

632   M2 sites labeled. The easy glide plane for dislocations gliding on (010) is marked. Visualization
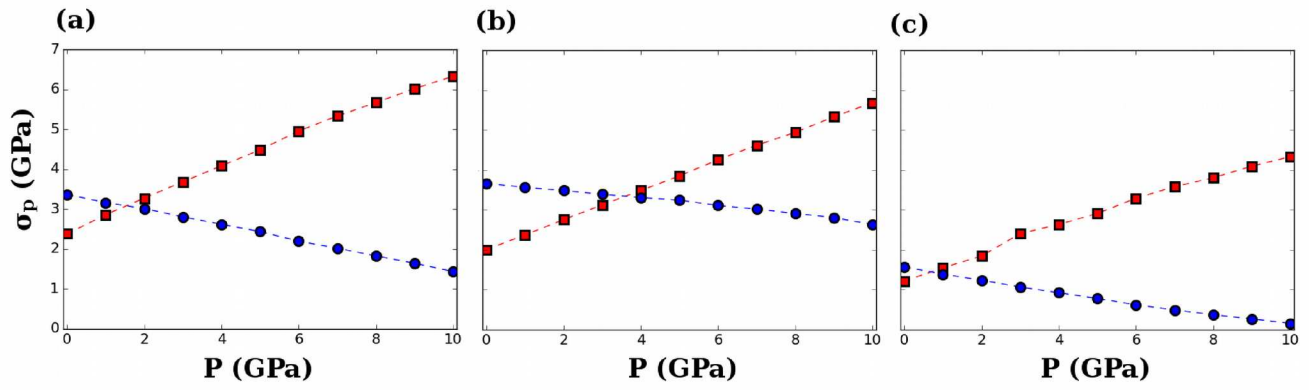
633   produced using VESTA 3 (Momma and Izumi 2011).

634
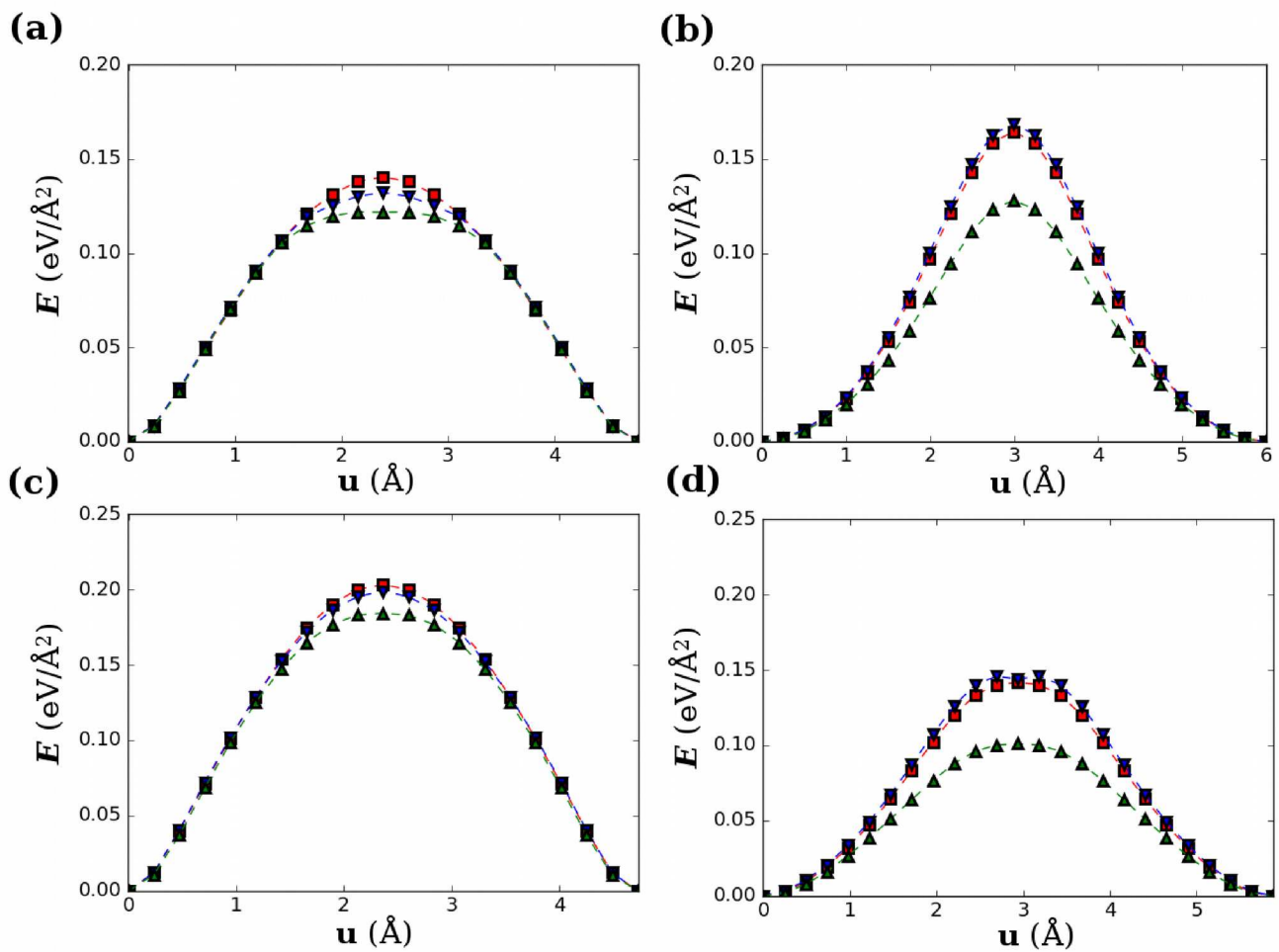
**Fig. 2** (a) [100](010) and (b) [001](010) γ-lines at 0 GPa. (c) [100](010) and (d) [001](010) γ-lines at 10 GPa. Square, triangle, and inverted triangle symbols correspond to GSFs without point defects, with $\{V_{M2}\}''$ defects, and with $\{V_{M1}\}''$ defects.
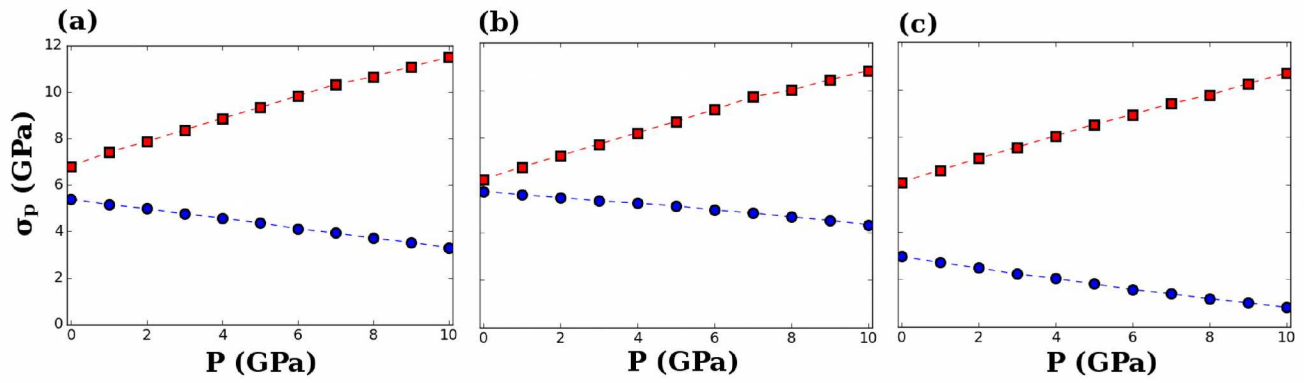
638
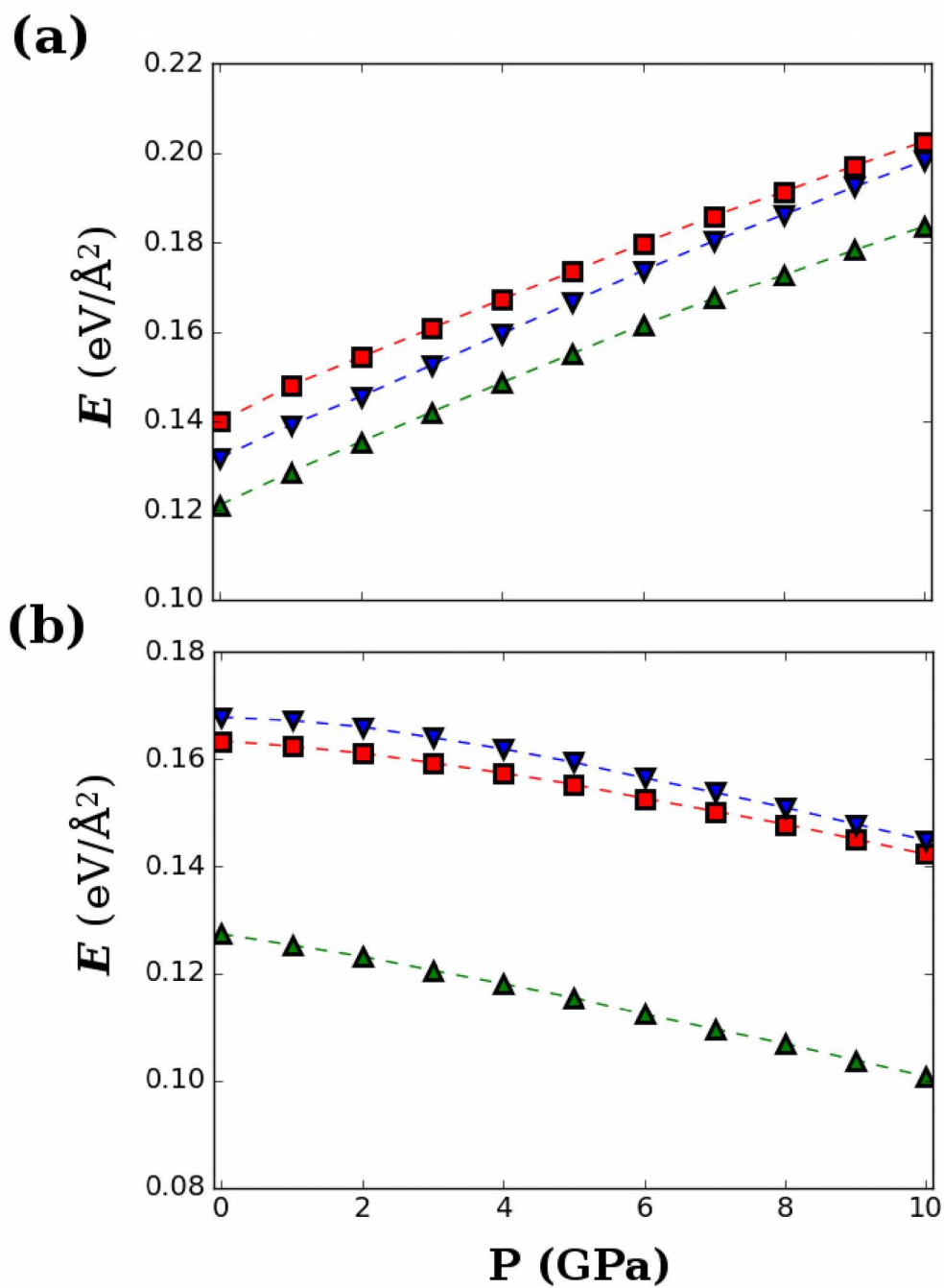
**Fig. 3** Maximum energies along the (a) [100](010) and (b) [001](010) γ-lines. Symbols have the same

meaning as in Fig. 2.

641

**Fig. 4** Pressure evolution of $\sigma_p$ for (squares) $[100](010)$ and (circles) $[001](010)$ edge dislocations with (a) no point defects, (b) a $\{V_{M1}\}''$ defect, and (c) a $\{V_{M2}\}''$ defect at the glide plane. All Peierls stresses are plotted using the same scale.

645

**Fig. 5** Pressure evolution of $\sigma_p$ for (squares) [100](010) and (circles) [001](010) screw dislocations with (a) no point defects, (b) a $\{V_{M1}\}''$ defect, and (c) a $\{V_{M2}\}''$ defect at the glide plane. All Peierls stresses are plotted using the same scale.

649
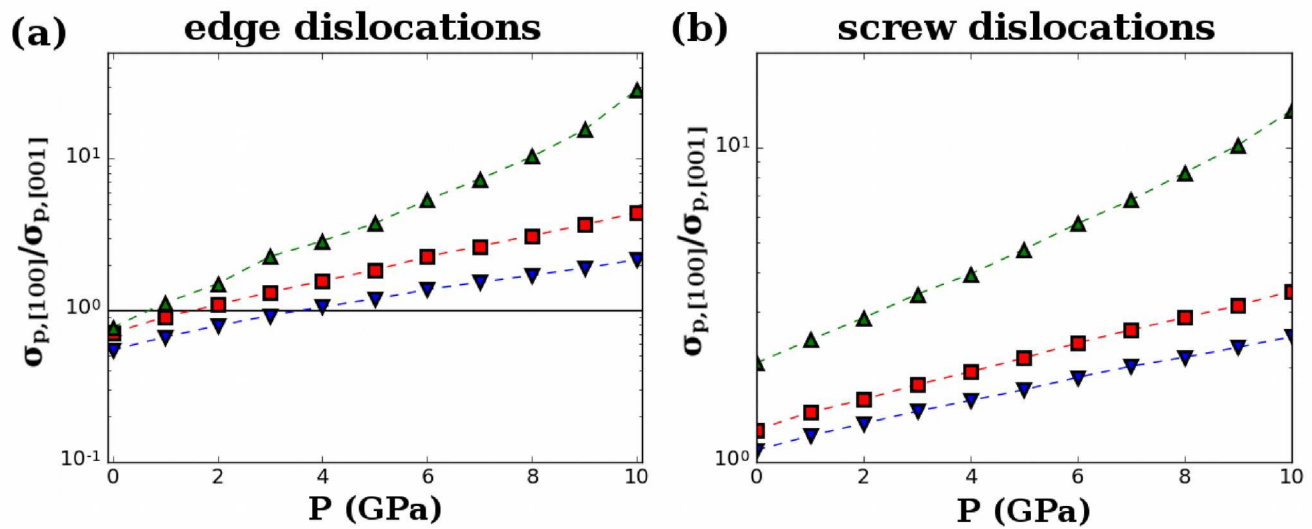
**Fig. 6** $\sigma_{p,[100]}/\sigma_{p,[001]}$ ratios for (a) edge, and (b) screw dislocations. Square, triangle, and inverted triangle

symbols correspond to GSFs without point defects, with $\{V_{M2}\}''$ defects, and with $\{V_{M1}\}''$ defects.